Growth dynamics and strain relaxation mechanisms in BaTiO$_3$ pulsed laser deposited on SrRuO$_3$/SrTiO$_3$

J. Q. He,[1,3,]* E. Vasco,[2] R. Dittmann,[1] and R. H. Wang[3]

[1]*Institut für Festkörperforschung, Forschungszentrum Jülich GmbH, D-52425 Jülich, Germany*
[2]*Instituto de Ciencia de Materiales de Madrid, Consejo Superior de Investigaciones Científicas, 28049 Cantoblanco, Madrid, Spain*
[3]*Physics Department and Center for Electron Microscopy, Wuhan University, Wuhan 430072, China*

The atomic structure of epitaxial BaTiO$_3$ films grown on SrRuO$_3$-covered (001)SrTiO$_3$ substrates by pulsed laser deposition has been studied by transmission electron microscopy. It revealed a three-layered structure, each layer with a different morphology, remaining strain, and density of defects. These results pointed to the existence of two growth regimes with distinctive strain-relaxation mechanisms: (i) A first dislocation-free layer extending 3 nm from the coherent interface with SrRuO$_3$. (ii) Beyond it, a second 7 nm thick semicoherent layer exhibiting a high density of misfit dislocations with a Burger vector $a\langle010\rangle$. The structures of both layers are the outcome of a two-dimensional layer-by-layer growth regime. (iii) A third layer extending throughout the rest of the BaTiO$_3$ film, showing a columnar structure of stoichiometric grains encapsulated by amorphous Ti-enriched boundaries, as disclosed by energy-dispersive x-ray spectroscopy. The structure of this third layer reflects its three-dimensional-featured growth habit. By considering both regimes as a single mode, the growth dynamics of the BaTiO$_3$ films is discussed in relation to strain-relaxation mechanisms potentially responsible for the Stranski-Krastanov growth mode of this system.

PACS number(s): 68.55.−a, 68.37.Lp, 77.55.+f

I. INTRODUCTION

A good deal of effort developed by the scientific community during the last years has gone into understanding the atomic mechanisms governing the growth kinetics and the kinetic roughness of functional materials grown in the form of thin films from the vapor phase by non-equilibrium techniques. Nevertheless, the attention paid to the complex oxides in this regard is rather little despite increasing interest in them due to their attractive functional (e.g., see progress on high-T_c superconductors,[1] magnetoresistors,[2] ferroelectrics,[3] and atomically perfect oxide gates on massive semiconductors[4]). Moreover, the exploration of the inherent mechanisms, underlying the growth of heteroepitaxial oxide systems, including those connected with strain relaxation, is straightforwardly insufficient. In this framework, the present work is intended to fill this gap by providing new data and insights on the far-from-the-equilibrium growth kinetics of epitaxial perovskite oxides.

The system's thermodynamic characteristics (e.g., free surface and interface energies, condensation energies, and strain energy) as well as its tendency toward minimum energy states (termed growth dynamics hereafter) determine the prevailing growth mode. Three major growth modes have been extensively described in the literature: (i) Two-dimensional (2D) layer-by-layer growth (also known as the Frank der Merwe mode[5,6]), (ii) three-dimensional (3D)-featured growth (Volmer-Weber[7]) and (iii) a mode starting as 2D and then turning into 3D growth (Stranski-Krastanov[8]). Recently, a fourth growth mode based on electronic confinement effects (electronic mode) was suggested.[9] In particular, the Stranski-Krastanov growth mode is commonly found in systems with low interface energies (such as semiconductors and oxides) and moderate lattice misfits (lower than 7% ac-

cording to the classical growth theory[10]). Under these conditions, coherent 2D growth is energetically favorable for films below a certain threshold thickness (the Stranski-Krastanov crossover thickness) from which the increasing energy ascribed to the lattice misfit strain leads toward a transition to a 3D-featured growth regime. Currently, the Stranski-Krastanov growth mode is largely used as an engineering tool to promote the self-organized and self-patterned growths of inorganic systems at the nanoscale level (see progress on quantum dots and strain-induced self-organization[11,12]). The growth dynamics takes place through the transition of the system between close kinetic states, wherein states far from the equilibrium could be stable for long periods (i.e., metastable[13]). Thus, the coexistence of "dynamic states"—namely those whose structures and morphologies are induced by the growth modes described above—with kinetic states is feasible.[14] This coexistence would be driven by the competition between the operating growth mechanisms and/or those of strain relaxation in both the particular system and the deposition technique used.

In this work, we investigated by standard and high-resolution transmission electron microscopy (TEM and HTEM, respectively) the atomic structure of BaTiO$_3$ (BTO) thin films deposited by pulsed laser on SrRuO$_3$ (SRO)/ SrTiO$_3$ (STO). Our structural analysis sheds light on the underlying growth mechanisms responsible for the strain relaxation in epitaxial BTO and related perovskite oxides.

II. EXPERIMENTAL METHODS

Epitaxial [001]BTO/[001]SRO bilayers (indexes referred to the pseudocubic SRO unit cell) were grown *in-situ* on commercial single-crystalline (001)STO substrates by pulsed laser deposition (PLD). The following parameters corre-
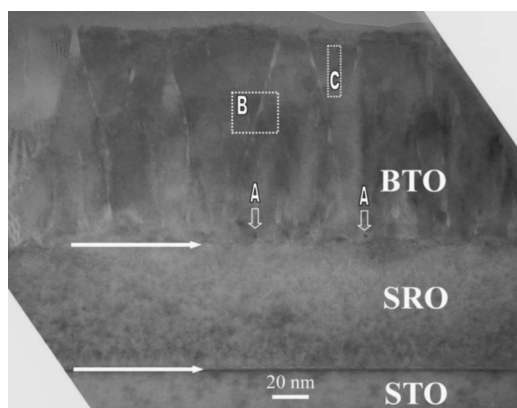
FIG. 1. Low-magnification cross-section image of a 120 nm BTO/70 nm SRO/STO heterostructure. Both the BTO/SRO and SRO/STO interfaces are marked by horizontal arrows. Labels *A*, *B*, and *C* denote misfit dislocation, grain boundary, and antiphase domain regions, respectively.

spond to the used experimental setup: KrF excimer laser ($\lambda = 248$ nm, 16 ns pulses, $\gamma = 10$ Hz) was focalized onto stoichiometric ceramic targets (first SRO, and then BTO, both rotating at 20 rpm) at a power density of 5 J/cm^2. The 70 nm thick SRO layer was deposited at 700 °C in an oxygen dynamic pressure of 25 Pa. Subsequently, the BTO films were grown at 5 Pa and the same temperature.

Cross-sectional and plan-view specimens were prepared for TEM observations by standard methods reported elsewhere.[15] TEM and HRTEM observations were made using Philips CM20-FEG and JEOL 4000EX microscopes. The TEM images were numerically simulated[16] to facilitate the structural analysis described below. The chemical composition of the BTO film was spatially resolved by means of an *in-situ* energy-dispersive x-ray spectroscopy (EDS) detector.

III. EXPERIMENTAL RESULTS

Figure 1 shows a low-magnification cross-sectional image of a 120 nm thick BTO film. The film forms an atomically flat interface with the SRO buffer layer and exhibits a rough top surface. Vertical arrows labeled as *A* point out to misfit dislocations within near-BTO/SRO interface regions with misfit strain gradients, as revealed by the image contrast. Several lighter oblique lines (denoted as *B*), which are originated far from the BTO/SRO interface, run up through the thickness of the BTO film to reach the top surface. These lines (as discussed below) are identified as boundaries between columnar-shaped grains. Other lines running parallel to the direction of growth (as that enclosed in *C*) are ascribed to antiphase domain (APD) defects. Details of the regions denoted as *A*, *B*, and *C* are given below.

The atomic-resolution image of a near-BTO/SRO interface region (region *A* in Fig. 1) is depicted in Fig. 2. The misfit dislocation pointed out in Fig. 2(a) has formed 3 nm away from the BTO/SRO interface. A Burgers circuit enclosing the dislocation core (not shown) would exhibit a closure failure of one lattice parameter along [010] BTO, which corresponds to a dislocation Burgers vector $a\langle010\rangle$. The varia-
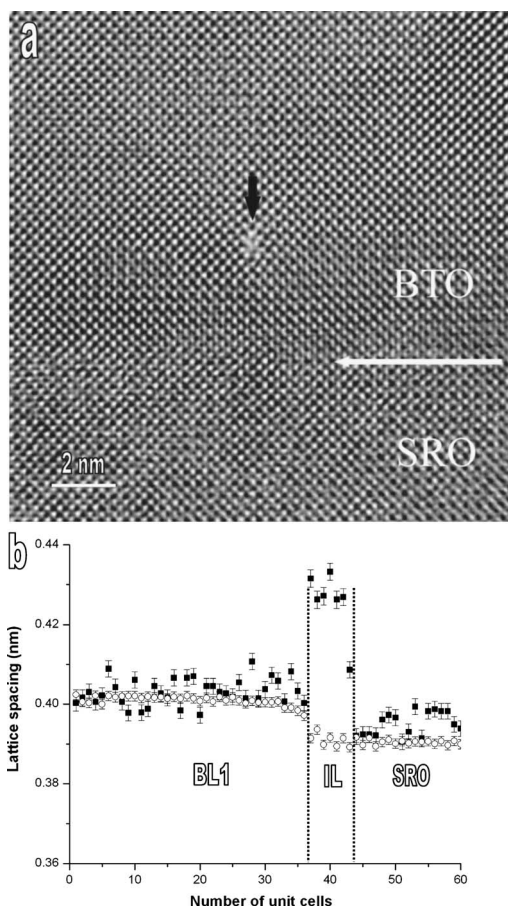

FIG. 2. (a) Atomic-resolution image of the near-BTO/SRO interface region; the zone axis is along [100] BTO. Horizontal and vertical arrows point to the interface and a misfit dislocation, respectively. (b) Evolution of the in-plane (open circles) and out-of-the-plane (solid squares) lattice parameters with the depth along the out-of-the-plane direction. Labels IL and BL1 denote the interfacial and bulk layer, respectively.

tion of the out-of-the-plane and in-plane lattice parameters (c_{BTO} and a_{BTO}, respectively) with the depth measured from the BTO/STO interface, and represented in unit cells from the cation positions was calculated by direct lattice mapping on the high-resolution image [Fig. 2(a)]. For this purpose, we applied a numerical center-of-mass approach taking the out-of-the-plane SRO lattice parameters (estimated below) as the calibration standard was applied. The results of such an analysis are depicted in Fig. 2(b). They reveal that the a_{BTO} lattice parameter (open circles) presents a discontinuity at 3 nm away from the interface within the BTO side; a_{BTO} being similar to the SRO lattice parameter within layer laying directly on the interface (termed the interfacial layer hereafter) and ≈ 0.401 nm for the rest of the BTO film (bulk layer). On the other hand, the c_{BTO} lattice parameter (solid squares) exhibits two discontinuities across both BTO/SRO and bulk layer/interfacial layer interfaces; the average c_{BTO} being 0.425 nm and 0.403 nm within the interfacial and bulk layers, respectively. The inner interface between the interfacial and bulk layer corresponds to the region where the misfit dislocations are gestated. The above analysis discloses that the dislocation-free 3 nm thick interfacial layer remains in a
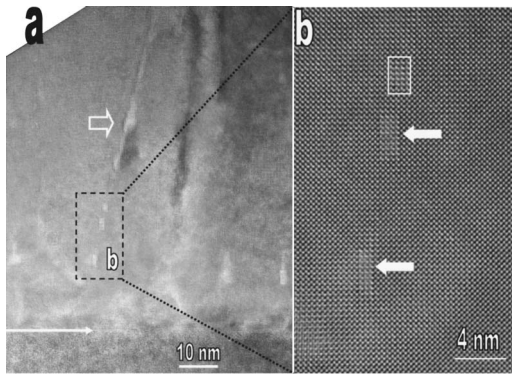
FIG. 3. (a) Medium-magnification cross-section image of a grain boundary region. The open arrow indicates the boundary. (b) Lattice image of the region enclosed in frame *B*. Solid arrows point to tetragonal-shaped defects. The zone axis is along [100] BTO.

highly strained state, exhibiting a compressive misfit strain as high as -2.9%, whereas the bulk layer mostly remains relaxed. The expansion of the c_{BTO} lattice parameter within the interfacial layer is a consequence of the compressive biaxial stress in the BTO/SRO interface due to the epitaxial lattice mismatch.

The medium-magnification cross-section image of a grain boundary (region *B* in Fig. 1) is shown in Fig. 3(a). The boundary originates ≈ 10 nm away from the BTO/SRO interface (i.e., 7 nm beyond the inner interface) and crosses the entire BTO film. Figure 3(b) displays high-resolution details of the region underneath the beginning of the grain boundaries. In this region, tetragonal-shaped defects with diffuse backgrounds are detected, having an average characteristic size of $3.5 \times 1.5 \times 1.5$ nm^3 and with their main axes lying along [001] BTO. Their diffuse backgrounds indicate that a non-negligible fraction of the volume of such defects is amorphous; this finding contrasts with the interpretation suggested by Zhu *et al.*[17] who described similar defects in $(Ba, Sr)TiO_3$ on $(La, Sr)CoO_3/LaAlO_3$ as aligned rectangular-shaped voids. The fact that the tetragonal defects are aligned with the grain boundary [marked by the open arrow in Fig. 3(a)] identifies them as early sections of such a boundary. The appearance of the climbing grain boundaries suggests they are crystalline disordered (but amorphous). The region where the boundaries form divides the bulk layer into two sublayers with different morphologies: a 7 nm thick compact sublayer that extends beyond the interfacial layer and exhibits a high density of misfit dislocations, and a columnar-structured sublayer for the rest of the BTO film. The difference between the morphologies of both sublayers indicates their dissimilar origins.

Figure 4(a) shows a selected-area electron diffraction (SAED) pattern along the [100] BTO zone axis acquired using an aperture that simultaneously collects diffractions coming from the BTO film, the SRO buffer layer, and the STO substrate. Three clearly distinct split diffracted spots are detected along the out-of-the-plane direction [Fig. 4(b)], whereas only two spots are perceptible in-plane direction [Fig. 4(c)]. An accurate image calibration employing digital micrograph processing software on the basis of assuming the cubic STO lattice parameter ($a_{STO}=0.3905$ nm) as a calibra-
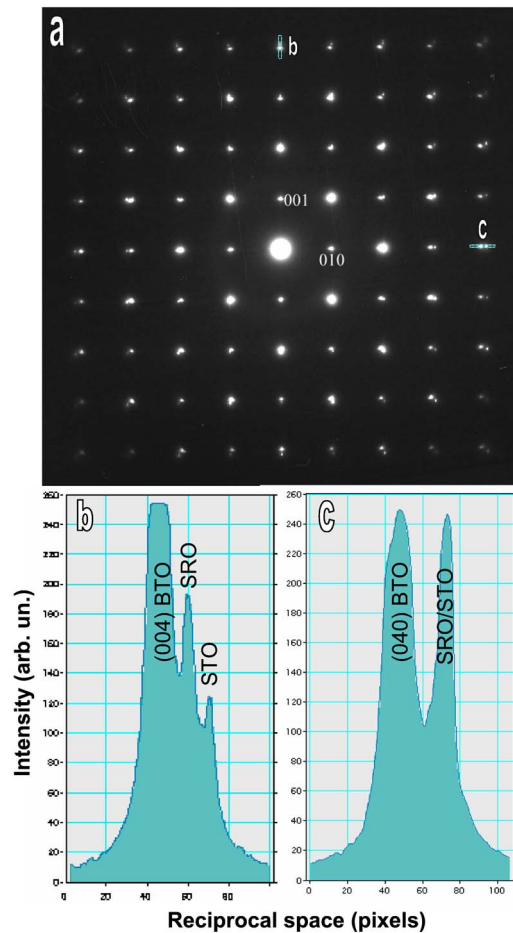

FIG. 4. (Color online) (a) SAED pattern along the [100] BTO zone axis resulting from simultaneous diffractions coming from BTO, SRO, and STO. (b) and (c) distributions in the reciprocal space of the diffractions along the out-of-the-plane ([001] BTO) and in-plane ([010] BTO) directions, respectively.

tion standard allows us to determine the bilayer in-plane ($a_{BTO}=0.4022$ nm and $a_{SRO}=0.3905$ nm) and out-of-the-plane ($c_{BTO}=0.4026$ nm and $c_{SRO}=0.3955$ nm) lattice parameters. These results, which agree with those in Fig. 2, indicate that the SRO buffer layer remains under compressive strain owing to the constrictions imposed by the substrate lattice, whereas the BTO film is mostly relaxed, with the main contributions to the electron diffraction being those coming from both BTO bulk sublayers. The nominal lattice misfits for the BTO/SRO/STO heterostructure can be computed from the preferential orientation of each film or layer and its corresponding bulk parameters (i.e., for [001]-oriented BTO, $a_{BTO}=0.4006$ nm; slightly distorted perovskite SRO with a pseudocubic unit cell, $a_{SRO}=0.3924$ nm; and cubic STO, $a_{STO}=0.3905$ nm). Thus, the nominal misfits estimated for both the (001)BTO/(001)SRO and (100)SRO/(001)STO interfaces are -2.0% and -0.48%, respectively. Because massive relaxation mechanisms do not exist within the SRO buffer layer, the misfit strain detected in BTO interfacial layer (-2.9%)—which is higher than that predicted for a coherent BTO/SRO interface—corresponds to the nominal misfit strain for a virtual BTO/STO interface. Such a lattice
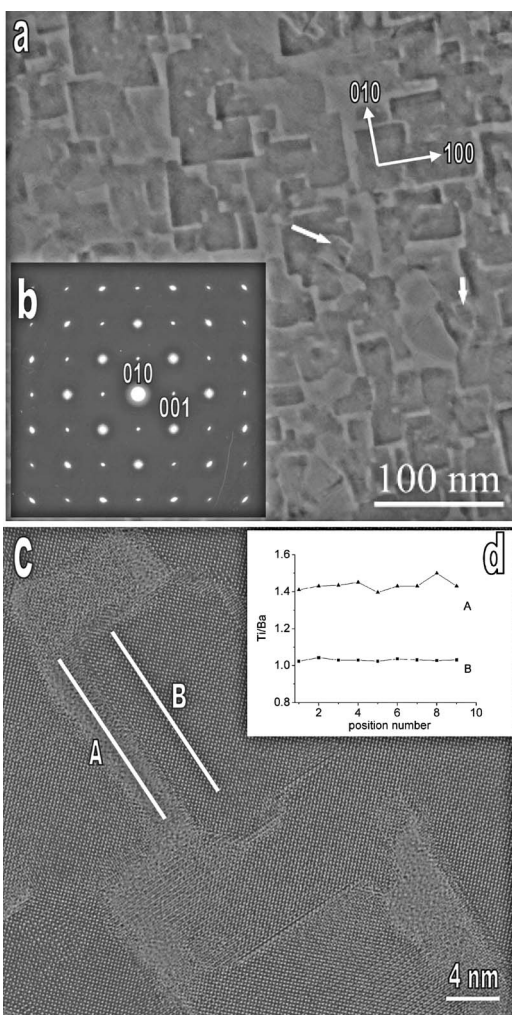
FIG. 5. (a) Low-magnification top view image of the outermost BTO layer. Arrows point to some in-plane misaligned grains. (b) SAED pattern from a surface area covered by a large number of columns. (c) High-resolution details of grain boundaries. The cation ratio (Ti/Ba) profiles depicted in (d) were obtained by EDS along lines *A* and *B* in (c).
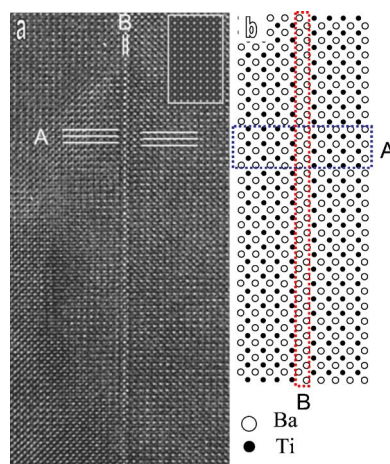

FIG. 6. (Color online) Lattice image (a) and schematic atomic representation (b) of two crossing antiphase domain defects within the bulk of a BTO columnar grain. *A* and *B* denote conservative and nonconservative domains, respectively. Inset, numerical simulation of the lattice image shown in (a).

misfit is accommodated through several mechanisms, the commonest ones being the following: by the remaining misfit strain, via the formation of misfit dislocations at the interfaces depending on the elastic properties of the in-contact materials and the growing film's thickness, or by a transition toward a 3D-featured growth habit as predicted for the Stranski-Krastanov growth mode. From the diffraction pattern in Fig. 4 and the dislocations, tetragonal defects and grain boundaries imaged in Figs. 2 and 3, we concluded that the BTO bulk layer is mostly relaxed via the formation of: (i) a network of misfit dislocations within the inner sublayer, (ii) tetragonal defects acting like incipient grain boundaries at the interface between both bulk sublayers, and (iii) amorphous grain boundaries within the outermost sublayer.

A top overview of the outermost BTO layer is depicted in Fig. 5(a). The orthogonal-shaped cross sections of the columnar grains are clearly visible with their main axes along the [100] and [010]BTO directions. The SAED pattern [Fig. 5(b)] obtained for a surface area covered by a large number of columns indicates common in-plane and out-of-the-plane orientations for all the columns, with a small fraction of in-plane misaligned grains. Some of these latter grains are indicated in Fig. 5(a). The grains are encapsulated by thick grain boundaries, which are imaged with high-resolution in Fig. 5(c). The amorphism of the grain boundaries is confirmed. Some dislocations or defects (as discussed below) are observed within the grain bulk. Figure 5(d) shows the cation ratio (Ti/Ba) profiles measured by EDS in the boundary (along line *A*) and grain bulk (line *B*) regions. The grain bulk is stoichiometric with a cation ratio Ti/Ba ≈ 1.03 close to that expected for perovskite oxides (Ti/Ba=1); whereas the grain boundaries exhibit nonperovskite ratios Ti/Ba ≈ 1.4 larger than the threshold of allowed stoichiometric defects for the perovskite phase existence. These nonstoichiometric Ti/Ba ratios indicate that the boundaries are largely Ti enriched (probably by amorphous TiO_x) compared to the composition of the grain bulk region.

Other kinds of defects (i.e., antiphase domains, APDs, as that enclosed in *C*, Fig. 1) appear within the bulk of the BTO columnar grains. Figure 6(a) shows the lattice image and its simulation (*inset*) of a grain bulk region containing two crossing antiphase domains: a conservative and a nonconservative one labeled as *A* and *B*, respectively. Figure 6(b) corresponds to a schematic representation of both APDs, showing their atomic structures. The formation of APDs acts as a complementary mechanism to release local strains[18] and/or growth instabilities (such as chemical faults[19]) induced by kinetic limitations.

IV. DISCUSSION

The existence of a dislocation-free highly strained interfacial layer in epitaxial perovskite oxides was previously observed in $(Ba,Sr)TiO_3$ (BST) films stacked between SRO electrodes on (100)STO substrates.[15] The nature of this interfacial layer was ascribed there to oxygen deficiencies acting

as kinetic limitations preventing the formation and/or propagation of misfit dislocations.[20] Such nonstoichiometric deficiencies would be originated during early growth stages as a complementary strain relaxation mechanism[21,22] for coherent films whose thicknesses would be smaller than the critical thickness above which the formation of misfit dislocations becomes energetically viable. Mader and Knauss[23] proposed, alternatively, that the origin of the interfacial layer lies in the balance between image forces arising from (i) the difference between film's and substrate's elastic properties, and (ii) coherency forces in the dislocations. Accordingly, their model predicts an increase in the thickness of the interfacial layer as the lattice mismatch decreases.[24] Our results, presented here and elsewhere,[15] are not strictly consistent with this prediction as follows: The thicknesses of the interfacial layers observed in (001)BST/(001)SRO and (001)BTO/(001)SRO are roughly similar ($\pm 10\%$) despite the large difference between the lattice mismatches of both systems; -0.9% and -2.9%, respectively. A possible explanation for this unpredicted behavior could be given by suggesting that there is a large change in the elastic properties and/or the bond strength for BTO as the substitution of Ba by Sr proceeds. In this regard, a reliable model would be needed to account for several factors that, in these systems, prevent the propagation of the misfit dislocations and stabilizes the lattice distortion.

The results reported here reveal that epitaxial BTO grows on SRO-covered STO according to the Stranski-Krastanov mode with particularities induced by the operating strain-relaxation mechanisms under the deposition conditions employed, which determine the balance between the system's kinetic limitations and thermodynamic tendencies. The growth stages (sketched in Fig. 7) are described in terms of the structural evolution, density and kind of defects, and the strain remaining within the BTO film as follows:

(a) The ultrathin film of BTO grows coherently on (001)SRO with a 2D layer-by-layer growth habit, giving rise to a lattice-coherent BTO/SRO system. The lattice mismatch in this system is accommodated depending on the energy balance either via lattice strain and/or by relaxation mechanisms available during early growth stages such as the creation of point defects (e.g., formation of oxygen vacancies), perturbations in the film surface morphology (e.g., increasing the surface roughness or modulating it periodically).

(b) The lattice strain energy (ε_s) rises as the BTO film thickness increases ($\varepsilon_s \propto d$), and the lattice-coherent BTO/SRO systems becomes unstable because the above relaxation mechanisms are insufficient to fully relieve highly strained states. Once the accumulated strain energy is larger than that required for the formation of misfit dislocations, which occurs for film thicknesses exceeding a threshold (critical thickness, d_c), the system is "macroscopically" relaxed via the creation of such dislocations. However, at the atomic scale, this mechanism introduces local lattice distortions so breaking down the homogeneity of the strain field within the BTO film bulk.[25] Thus, the near-misfit dislocation regions, including those seated directly on the dislocation sites (as reported elsewhere[15]) remains mostly relaxed, whereas the interdislocation regions continue to be partially strained. Thus a BTO film thicker than d_c grows in a 2D layer-by-layer semicoherent manner.
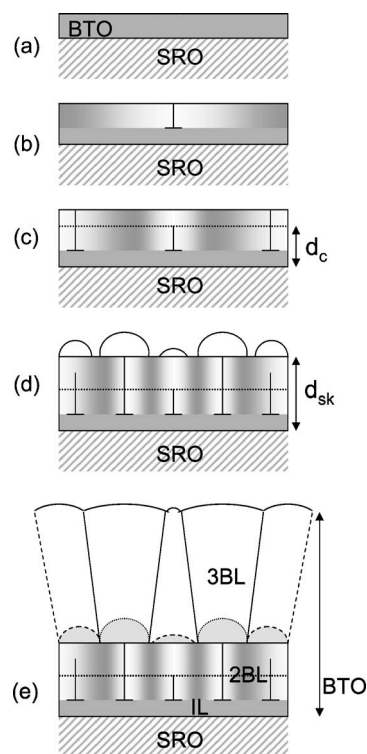

FIG. 7. Schematic representation of different stages in the structural evolution of the epitaxial BTO film: (a) Highly strained film under the critical thickness (d_c) for the formation of misfit dislocations. (b) and (c) Increase of the density of misfit dislocations as the film thickness increases within the range from d_c to d_{SK}. The dislocations originate several nanometers away from the BTO/SRO interface and climb up toward the film surface. (d) 2D growth habit is replaced by a 3D-featured one for film above the Stranski-Krastanov thickness (d_{SK}). 3D nuclei are formed on the relaxed surface areas. (e) Columnar growth taking place from the incomplete coalescence of the 3D nuclei. The gray level represents the remaining strain level within the BTO film, which exhibits a layered structure formed by an interfacial layer (IL) and a bulk layer (BL). The latter is subdivided into two sublayers with 2D (2BL) and 3D (3BL) featured morphologies.

(c) As growth proceeds, new dislocations nucleate ($\propto 1 - d_c/d$). However, the available maximum density of misfit dislocations is limited by kinetic factors as, for example, interactions between dislocations that are close together.[26,27] So, further growth on the strained interdislocation regions causes a transition toward 3D-featured growth as the formation of dislocations ceases to be an efficient relaxation mechanism. Such a transition happens for the BTO film thicker than a second critical value, termed the Stranski-Krastanov thickness (here, $d_{SK} \approx 10$ nm). The transition takes place gradually from the formation of 3D nuclei on the relaxed surface areas (i.e., those seated on dislocation sites).

(d) Incomplete coalescence of 3D nuclei on the strained areas first triggers the formation of crystalline defects during the initial stages of coarsening, and subsequently, the development of grain boundaries from these defects. Hence, it is likely that the buried tetragonal-shaped defects [shown in Fig. 3(b)] result from the migration and partial coalescence of the early grain boundaries. Further growth gives rise to a

fully relaxed BTO film with a columnar structure evolving according to the 3D-featured growth habit. Extra strain induced by stoichiometric defects, coalescence of the single-crystalline regions, and competition by the lateral space between columnar grains, for example, is relaxed via complementary mechanisms such as the formation of antiphase domains[18] (Fig. 6). Since the growth proceeds from stoichiometric BTO targets, the Ti enrichment of the grain boundaries (and likely that of the tetragonal-shaped defects as incipient boundaries) is due to the segregation of excess Ti towards these regions as a result of the perovskite-phase crystallization in a Ba concentration-limited regime. Such a regime would be induced by Ba losses connected with inherent phenomena in the growth by PLD,[28] such as the incongruent target evaporation so that its surface is progressively enriched in heavy elements, preferential scattering within the ablation plasma or differential sticking coefficient per incident species.

The 3D growth habit is directly responsible—even at high temperature—for the relatively high surface roughness of the BTO films, since it describes the dynamics of highly mismatched systems in which misfit strain energy is lowered by an increase in their surfaces to attain a favorable balance between strain energy and free surface tension.[29] Furthermore, grain coalescence via boundary migration and/or recrystallization occurring at high temperature also is partially inhibited by the system's dynamics. On the other hand, since the origin of the interfacial layer can be ascribed to oxygen deficiencies, the highly strained state of this layer would correspond to a kinetic state rather than a dynamic one. Such a state could hardly revert through reoxygenation process at high temperature, but in any case, it would coexist with the Stranski-Krastanov growth mode imposed by the system's dynamics.

V. CONCLUSIONS

The growth mode (i.e., growth dynamics) of epitaxial $BaTiO_3$ deposited on $SrRuO_3$-covered $SrTiO_3$ by PLD was investigated at atomic scale by TEM and HRTEM. $BaTiO_3$ grows according to a Stranski-Krastanov mode ruled by several strain relaxation mechanisms, which operate in a complementary way giving rise to a layered structure of the $BaTiO_3$ film. Major mechanisms (such as the formation of misfit dislocation networks and amorphous grain boundaries) and minor ones (the remaining lattice strain and the formation of antiphase domains) for epitaxial stress relief were identified at different growth stages. Besides the two layers predicted for a film growing according to the Stranski-Krastanov mode (i.e., a first layer exhibiting a 2D layer-by-layer growth, and the second one with a 3D-featured growth) a distinctive highly strained interfacial layer—with a probable kinetic origin—was detected. The latter suggests that both kinetic and dynamic states coexist in this highly mismatched system.

*Present address: Center for Functional Nanomaterials, Bldg. 480, Brookhaven National Laboratory, Upton, NY 11973, USA. Electronic address: jhe@bnl.gov

[1] D. Dijkkamp, T. Venkatesan, X. D. Xu, S. A. Shaheen, N. Jisrawi, Y. H. Min-Lee, W. L. McCean, and M. Croft, Appl. Phys. Lett. **51**, 619 (1987).

[2] R. von Helmolt, J. Wecker, B. Holzapfel, L. Schultz, and K. Samwer, Phys. Rev. Lett. **71**, 2331 (1993).

[3] J. S. Horwitz, K. S. Grabowski, D. B. Chrisey, and R. E. Leuchtner, Appl. Phys. Lett. **59**, 1565 (1991).

[4] H. Lee, D. Hesse, N. Zakharov, and U. Gösele, Science **296**, 2006 (2002).

[5] F C. Frank and J. H. van der Merwe, Proc. R. Soc. London, Ser. A **198**, 205 (1949).

[6] J. H. van der Merwe, J. Appl. Phys. **34**, 117 (1963).

[7] M. Volmer and A. Weber, Z. Phys. Chem., Stoechiom. Verwandtschaftsl. **119**, 277 (1926).

[8] I. N. Stranski and L. von Krastanov, Akad. Wiss. Lit. Mainz Abh. Math. Naturwiss. K1.0002-2993 **146**, 797 (1939).

[9] D. A. Luh, T. Miller, J. J. Paggel, M. Y. Chou, and T. C. Chiang, Science **292**, 1131 (2001).

[10] J. W. Matthews, Philos. Mag. **6**, 1347 (1961); **13**, 1207 (1966).

[11] B. Voigtländer, Surf. Sci. Rep. **43**, 127 (2001) and references therein.

[12] C. Teichert, Phys. Rep. **365**, 335 (2002) and references therein.

[13] C. W. Snyder, B. G. Orr, D. Kessler, and L. M. Sander, Phys. Rev. Lett. **66**, 3032 (1991).

[14] Y. W. Mo, D. E. Savage, B. S. Swartzentruber, and M. G. Lagally, Phys. Rev. Lett. **65**, 1020 (1990).

[15] J. Q. He, E. Vasco, C. L. Jia, R. Dittmann, and R. H. Wang, J. Appl. Phys. **97**, 104907 (2005).

[16] TEM image numerical simulations were carried out with the MacTempas computer program with the following parameters as input: spherical aberration, defocus spread, semiconvergence angle of illumination and diameter of the objective lens aperture of 1 mm, 8 nm, 0.55 mrad, and 7 nm, respectively.

[17] X. Zhu, H. L.-W. Chan, C.-L. Choy, K.-H. Wong, and D. Hesse, J. Appl. Phys. **97**, 093503 (2005).

[18] W. Bogdanowicz, Mater. Sci. Eng., A **346**, 328 (2003).

[19] G. Van Tendeloo, O. I. Lebedev, and S. Amelinckx, J. Magn. Magn. Mater. **211**, 73 (2000).

[20] J. Q. He, E. Vasco, C. L. Jia, and R. H. Wang, Appl. Phys. Lett. **87**, 062901 (2005).

[21] D. A. Muller, N. Nakagawa, A. Ohtomo, J. L. Grazul, and H. Hwang, Nature (London) **430**, 657 (2004).

[22] E. Vasco, R. Dittmann, S. Karthäuser, and R. Waser, Appl. Phys. A: Mater. Sci. Process. **79**, 1461 (2004).

[23] W. Mader and D. Knass, Acta Metall. Mater. **40**, S207 (1992).

[24] V. Vitek, G. Gutekunst, J. Mayer, and M. Ruhle, Philos. Mag. A **71**, 1219 (1995).

[25] M. W. Chu, I. Szafraniak, R. Scholz, C. Harnagea, D. Hesse, M. Alexe, and U. Gosele, Nat. Mater. **3**, 87 (2004).

[26] J. W. Matthews and A. E. Blakeslee, J. Cryst. Growth **29**, 273 (1975).

[27] B. W. Dodson, J. Cryst. Growth **111**, 376 (1991).

[28] *Pulsed Laser Deposition of Thin Films*, edited by D. B. Chrisey and G. K. Hubler (Wiley, New York, 1994), Chaps. 4, 5, 7, and 9.

[29] D. J. Srolovitz, Acta Metall. **37**, 621 (1989).